Computational study of aluminum droplet combustion in different atmospheres

Muller Mathieu[1], Davidenko Dmitry[1], Giovangigli Vincent[2]
[1]ONERA, Chemin de la Hunière, 91123 Palaiseau, France
[2]Ecole Polytechnique, 91128, Palaiseau, France

Abstract

Combustion of a single aluminum droplet in different atmospheres is simulated using a 1D approach, recently developed at ONERA, with detailed models for the gas-phase and surface chemistry as well as molecular transport. The reacting flow around a droplet is treated as spherically symmetric and quasi-steady-state by assuming that the droplet regression is slow with respect to the convective and diffusive transport in the surrounding gases. The 1D combustion model is first validated with respect to the 2D axisymmetric approach. It is demonstrated that with the 1D approach, it is possible to take into account the effect of oxidizer convection and obtain parameter profiles closely corresponding to the 2D results. The results of both simulations are found in good agreement with available experimental data for an O_2/Ar atmosphere. Using the 1D approach, an important parametric study has been conducted by simulating steady combustion of droplets with different diameters $D \leq 400\,\mu m$ in three atmospheres (O_2/Ar, pure H_2O and CO_2) at two pressure levels (1 and 10 atm). Effects due to the surface chemistry model and the reversibility of the gas-phase reactions producing Al_2O_3(L) have been investigated. The burning time and exponent of the D^n law are evaluated for the considered physical conditions and modeling options. Profiles of temperature and mole fractions of important species are presented and analyzed.
Keywords: Aluminum droplet, combustion modeling, detailed chemical kinetics, surface reactions, numerical simulation, burning time

1. Introduction

Combustion of metals provides an important energy release and is widely used for propulsion purposes. In particular, aluminum particles are often introduced as an energetic component in solid propellant formulations to improve the specific impulse of solid rocket motors. Metal particles burn in a gaseous atmosphere and produce condensed-phase residues. This process need to be properly characterized in order to predict possible negative effects, for example thrust losses due to the dispersed phase. Detailed modeling of individual particle combustion can provide such a characterization but it is a challenging problem because it needs to take into account complex physico-chemical phenomena.

In combustion simulations, a modeling methodology based on solving the Navier-Stokes equations for an axisymmetric steady-state reacting flow around an aluminum droplet has been actively used since the 2000s. The evolution of the modeling approach can be seen from particular publications. A complete combustion model of an aluminum droplet in an oxygen-containing atmosphere was presented by Beckstead et al. [1] describing principal physico-chemical processes. Gas-phase and heterogeneous chemistry was represented by a number of global reactions. In particular, heterogeneous reactions were formulated for evaporation and oxidation on the droplet surface as well as for condensation and dissociation of liquid alumina. An expression for the rate of alumina condensation was derived from the nucleation theory. A simple model of dissociation threshold was used to limit the fraction of liquid alumina and, as a consequence, the flame temperature. Thermodynamic and transport properties of the gaseous phase were determined from the mixture components properties. A particular Schmidt number was introduced to treat the diffusion of liquid alumina particles. The Navier-Stokes equations were formulated for a 2D axisymmetric flow using the low-Mach assumptions. The droplet was represented by a constant-diameter sphere, with a segment occupied by the oxide cap to reduce the reactive surface.

This model was later improved by Washburn et al. [2] by replacing the global gas-phase reactions with a detailed kinetic mechanism developed by Catoire and Swihart. However, only Al evaporation was modeled by assuming

Muller Mathieu, Davidenko Dmitry, Giovangigli Vincent

the equilibrium vapor fraction at the droplet surface.

A detailed kinetic mechanism for the aluminum surface was recently developed by Glorian [3][4]. This surface mechanism together with the detailed gas-phase mechanism [2] was used by Glorian et al. [5] for simulations of the aluminum droplet combustion in different atmospheres with the CPS code developed at ASL. A 2D axisymmetric flow of a multispecies reacting gas was simulated around a constant-diameter aluminum droplet without oxide cap. Some important simplifications were adopted to treat the liquid alumina as an ideal gas in the equation of state and molecular transport model. Two global irreversible reactions converting the gas-phase alumina into the liquid phase were added to the gas-phase reaction mechanism.

At ONERA, numerical simulations of the aluminum droplet combustion in the 2D axisymmetric approach were performed by Orlandi in the early 2000s using the MSD code. In these simulations different gas-phase kinetic mechanisms were used first for the combustion in air [6] and then in the hot gases from a burnt solid propellant [7]. Later simulations of the aluminum droplet combustion for some particular conditions were made using a similar approach with the CEDRE code.

This short overview shows that the common practice consists in simulating a reacting flow around a constant-diameter spherical droplet in the 2D axisymmetric configuration. Alternatively, a 1D spherically-symmetric approach was proposed by Cho et al. [8] for simulating the droplet combustion with detailed models for the chemical kinetics and molecular transport. A numerical model based on this 1D approach was used by Bucher et al. [9] to simulate the aluminum droplet combustion by assuming partial equilibrium for the gaseous species.

A 1D combustion model was recently developed at ONERA to simulate the aluminum droplet combustion with detailed models for the chemical kinetics and molecular transport. The purpose of the present paper is to validate the 1D approach and present the simulations results for different physical conditions (oxidizer composition, ambient pressure, droplet diameter) and modeling assumptions (use of the surface chemistry, reversibility of the gas-phase reactions producing liquid alumina). For the conditions considered in this study, the diffusion-controlled regime of combustion is mainly obtained but one also can see the transition towards the kinetically-controlled regime at smaller droplet diameters. Nevertheless, the surface chemistry plays an important role even with the diffusion-controlled regime especially in the H_2O atmosphere.

2. Modeling methodology

The modeling approach used considers a spherical droplet in an oxidizing atmosphere by assuming infinite quantity of oxidizer. The reacting flow around the droplet is treated as steady-state, which supposes that the droplet regression is slow with respect to the convective and diffusive transport in the surrounding gases. The oxide cap and radiative heat losses are not taken into account in the current study.

Most of the results presented below were obtained using a 1D flow model, which treats the flow as spherically symmetric. This 1D model has been validated with respect to more complex cases of a 2D axisymmetric configuration. One of these validation cases will be considered in this paper. Both 1D and 2D approaches use the same thermochemical and transport models.

2.1 Thermodynamic model

Three phases are considered in the present model: gaseous, surface and bulk. The two last phases pertain to the droplet. Thermodynamic properties of any species are defined by specifying a molar mass, a temperature polynomial for the molar heat capacity at constant pressure as well as molar enthalpy of formation and entropy of formation. The thermodynamic model used in this study is the same as in [5].

2.2 Chemical kinetic model

Two kinetic models are used in this study: gas-phase and surface. As for the thermodynamic model, the kinetic models are taken from [5]. The full gas-phase and surface mechanisms include species with the N and Cl elements, which are not considered in the present study. To make the simulations faster, specific subsets of species and reactions are selected for the reacting systems corresponding to the specific oxidizer atmospheres considered below. The numbers of species and reactions included in the kinetic models for three systems are summarized in Table 1. For the surface reactions, the gaseous species are taken from the corresponding gas-phase mechanisms.

Table 1 – Characteristics of the kinetic mechanisms for different reacting systems.

Reacting system	Gas-phase mechanism		Surface mechanism		
	Gaseous species	Reactions	Surface species	Bulk species	Heterogeneous reactions
Al-O	10	15	6	2	25
Al-H-O	20	44	11	3	38
Al-C-O	12	19	9	3	33

For the gas-phase kinetic model, Glorian et al. introduced two global reactions producing liquid alumina $Al_2O_3(L)$ from gas-phase isomers Al_2O_3 and Al_2O_{3c}:

$$Al_2O_3 => Al_2O_3(L) \quad \text{and} \quad Al_2O_{3c} => Al_2O_3(L) \tag{1}$$
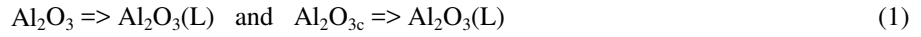
These two reactions are irreversible hence $Al_2O_3(L)$ cannot dissociate, which seems to be nonphysical at a temperature approaching 4000 K.

In this paper, reversible reactions will be also considered to introduce the effect of alumina dissociation:

$$Al_2O_3 <=> Al_2O_3(L) \quad \text{and} \quad Al_2O_{3c} <=> Al_2O_3(L) \tag{2}$$
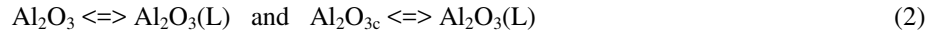
It should be noted that the rate constants used for reactions (1) and (2) are very high and do not limit the production of $Al_2O_3(L)$. This also means that reactions (2) are near equilibrium.

2.3 Molecular transport model

The results presented below were obtained with a molecular transport model similar to that described in [5]. Globally, transport coefficients and molecular fluxes are determined using approximate relations and by neglecting the Soret and Dufour effects due to thermodiffusion. With this approach, it will be possible to compare our results with those from [5]. More accurate modeling using precise determination of molecular fluxes with thermodiffusion has been also performed, whose results are reserved for future publications.

The model description provided here gives only main relations to allow identifying the differences with respect to the model from [5]. The diffusive mass flux of the kth species is defined by:

$$J'_k = -\rho \, Y_k D_k \nabla X_k \tag{3}$$

with ρ the density of the gas mixture, Y_k the mass fraction of the kth species, D_k the diffusion coefficient of the kth species in the gas mixture, and ∇X_k the gradient of species mole fraction. This expression is approximate so to guarantee that the sum of all the diffusive fluxes is 0, the following correction is introduced:

$$J_k = J'_k - Y_k \sum_{l=1}^{K_g} J'_l \tag{4}$$

where K_g is the number of gaseous species.

The molecular heat flux q contains diffusion and conduction (Fourier) terms:

$$q = \sum_{k=1}^{K_g} h_k J_k - \lambda \, \nabla T \tag{5}$$

with λ the thermal conductivity of the gas mixture, ∇T the temperature gradient, and h_k the mass-specific enthalpy of the kth species.

The transport properties are defined in the standard manner by specifying parameters of the potential function for pure species and by applying the classical formalism of the molecular kinetics theory. Transport coefficients D_k and λ are determined using the computational methods developed by Ern and Giovangigli [11][12].

For the particular validation case presented in section 3, the following approximation of thermal conductivity is used in the 2D and 1D simulations:

$$\lambda = \frac{1}{2}\left[\sum_{k=1}^{K_g} X_k \, \lambda_k + \left(\sum_{k=1}^{K_g} X_k/\lambda_k \right)^{-1} \right] \tag{6}$$

2.4 1D flow model

The governing equations describing a steady-state spherically-symmetric isobaric flow of reacting gas around a

Muller Mathieu, Davidenko Dmitry, Giovangigli Vincent

droplet are:

$$M \, \nabla h + \nabla(A \, q) = 0 \tag{7}$$

$$M \, \nabla Y_k + \nabla(A \, J_k) = A \, \dot{m}_k \tag{8}$$

The energy equation (7) contains convective and molecular transport terms. The species transport equations (8) include convective and diffusion terms, and a chemical source term. The mass flow rate $M = A \, \rho \, u$ is constant at every section, defined by the radial coordinate x, with $A = 4 \, \pi \, x^2$ the spherical surface area and u the flow speed. The gas density ρ is determined from the ideal gas law for a prescribed pressure in the surrounding atmosphere. The mass-specific enthalpy h is the sum of $Y_k \, h_k$ of all the gaseous species. $\dot{m}_k$ is the net production rate per unit volume of the kth species defined by the chemical kinetic model.

2.4.1 Boundary conditions

Boundary conditions are used to determine physical quantities M, T and Y_k on the droplet surface (inner boundary) and in the surrounding atmosphere (outer boundary). The droplet surface can be modeled as either reactive or nonreactive.

For the reactive droplet surface, the boundary conditions cannot be directly specified in terms of physical quantities. The surface conditions are determined by satisfying balance relations for mass and thermal fluxes. The mass flux balance equation for the kth gaseous species is:

$$\rho \, Y_k \, u + J_k = -\dot{s}_{k,g} \tag{9}$$

$\dot{s}_{k,g}$ is the net rate of mass production per unit surface due to heterogeneous reactions. The convection velocity u, called the Stefan velocity is defined by:

$$u = -\frac{1}{\rho} \sum_{k=1}^{K_g} \dot{s}_k \tag{10}$$

The surface species are considered at equilibrium so the following condition must be verified for the net production rates of these species:

$$\dot{s}_{k,s} = 0 \tag{11}$$

Among the bulk species, liquid aluminum Al(L) is the only one which is consumed by the surface reactions and its fraction in the droplet is taken equal to 1 by neglecting the other bulk species generated by the surface reactions.

In steady state, the droplet temperature is homogeneous so there is no heat transfer inside the droplet. Hence, the thermal flux balance on the surface can be written:

$$-(\lambda \, \nabla T)_g = \sum_{k=1}^{K_{tot}} \dot{s}_k \, h_k \tag{12}$$

The heat conduction flux in the gas is on the left. Using (9), the production term on the right can be expressed:

$$\sum_{k=1}^{K_{tot}} \dot{s}_k \, h_k = \sum_{k=K_g+1}^{K_{tot}} \dot{s}_k \, h_k - \sum_{k=1}^{K_g} (\rho \, Y_k \, u + J_k) \, h_k \tag{13}$$

K_{tot} represents the total set of species in the three phases, where the gas-phase species are numbered from 1 to K_g.

For the nonreactive droplet surface, only aluminum evaporation is taken into account by assuming equilibrium between gaseous and liquid aluminum on the surface. Following Washburn et al. [2], the equilibrium mass fraction of gaseous aluminum is:

$$Y_{Al} = \frac{W_{Al} \, P_{Al}}{W \, P} = \frac{W_{Al} \, P°}{W \, P} \, \exp\left(\frac{S°_{Al} - S°_{Al(L)}}{R} - \frac{H_{Al} - H_{Al(L)}}{R \, T}\right) \tag{14}$$

where subscripts Al and Al(L) indicate gaseous and liquid aluminum respectively; the quantities corresponding to 1 atm are marked by "°"; W is the molar mass; P is the pressure; R is the universal gas constant; H and S are the molar enthalpy and entropy respectively. The surface mass flux of Al is:

$$\rho \, Y_{Al} \, u + J_{Al} = \rho \, u \tag{15}$$

and the surface fluxes of the other gaseous species are:

4

$$\rho \, Y_k \, u + J_k = 0 \tag{16}$$

The thermal flux balance on the surface is expressed by the following equation:

$$-(\lambda \, \nabla T)_g = \rho \, u \, (h_{Al(L)} - h_{Al}) \tag{17}$$

At the outer boundary, only the temperature and species mass fractions corresponding to the oxidizer atmosphere are imposed. These conditions are artificial being applied to a 1D steady flow but they are convenient for the following reasons: (i) the flowfield near the droplet does not depend on the distance to the outer boundary if it is sufficiently far; (ii) it is possible to take into account the effect of oxidizer convection by adjusting the distance to the outer boundary.

2.4.2 Solution procedure

Transport equations (7) and (8) are discretized in a conservative manner with the finite volume method. The convective fluxes can be approximated either by the 1st order upwind scheme or a hybrid scheme with variable upwinding depending on the local Peclet number. The molecular transport fluxes are approximated using the standard 2nd order central differencing. With these schemes, the finite difference equations are formulated for a 3-point numerical stencil.

Equations (7) and (8) in the discretized form with the boundary conditions represent a system of coupled nonlinear equations, which is solved by the Newton-Raphson method with a numerically evaluated Jacobian matrix. For stable convergence of the numerical iteration, optional temporal terms can be added to the solved equations then a nearly steady-state solution is obtained after a series of time steps.

Conditions (11) require a particular procedure to determine the equilibrium composition of surface species. Production terms $\dot{s}_{k,s}$ are functions of T and the species concentrations on the droplet surface. For some fixed T and gaseous species concentrations, the equilibrium composition of surface species can be obtained by solving a system of ordinary differential equations:

$$\frac{d \, \gamma_{k,s}}{d \, \tau} = \sigma_{k,s} \, \dot{s}_{k,s}/W_k \tag{18}$$

with $\gamma_{k,s}$ the surface molar density of the kth species, $\sigma_{k,s}$ the number of sites occupied by the kth species, W_k the species molar mass, and τ the pseudo-time variable. This system is numerically integrated up to convergence by a dedicated procedure, which is called every time the surface state is updated.

Solution errors due to spatial discretization are minimized by grid adaptation, which is performed a posteriori by controlling solution variation between grid nodes. The grid is refined by splitting grid intervals in the zones of important gradient and curvature of solution variables. Solution and grid refinement cycles are repeated until all the grid intervals are well adapted. Grid adaptation criteria are established empirically providing almost grid-independent solution with minimized number of grid nodes.

The 1D flow model is realized in a proprietary code written in Fortran 95. It uses specific libraries for calculating the thermodynamic properties, chemical production rates, and molecular transport coefficients. Gas-phase thermochemistry is processed by optimized routines derived from the CHEMKIN-II library. Surface thermochemistry is treated by the CHEMKIN-II standard routines. The molecular transport coefficients are determined using EGlib.

2.5 Burning time evaluation

Burning time is one of the primary characteristics of droplet combustion, which is often represented as a function of the initial droplet diameter D_0:

$$\tau_b = a \, D_0^n \tag{19}$$

Theoretically the value of n depends on the combustion regime: $n = 2$ for diffusion-controlled combustion with a detached gaseous flame around the droplet and $n = 1$ for combustion controlled by heterogeneous kinetics on the droplet surface. For aluminum particle combustion, Beckstead [10] proposed an empirical correlation with $n = 1.8$ and a coefficient dependent on the pressure, temperature, and fractions of oxidizer species O_2, H_2O and CO_2.

Muller Mathieu, Davidenko Dmitry, Giovangigli Vincent

To evaluate the burning time from simulation results, one can follow the method described by Glorian [3][5] and use the following expression:

$$\tau_b = \frac{\rho_{Al(B)}}{2} \int_0^{D_0} \frac{dD}{\dot{s}_{Al(B)}} \tag{20}$$

$\rho_{Al(B)}$ is the density of liquid aluminum in the bulk phase. $\dot{s}_{Al(B)}$ is the mass consumption rate of bulk aluminum by surface reactions. The method consists in approximating the integral in (20) from a series of computational results on $\dot{s}_{Al(B)}$ for different diameters.

The burning time interval between two simulated states defined by diameters D_1 and D_2 can be evaluated by linearizing the evolution of $\dot{s}_{Al(B)}^{-1}$ and applying the trapezoid rule:

$$\tau_{b_1} - \tau_{b_2} = \frac{\overline{\rho_{Al(B)}}}{2} \, \overline{\dot{s}_{Al(B)}^{-1}} (D_1 - D_2) \tag{21}$$

$\overline{\rho_{Al(B)}}$ is the mean value of bulk density, which depends on the droplet temperature according to the correlation by Marion and al. [13]:

$$\rho_{Al(B)}[\text{kg m}^{-3}] = 3236 - 0.604\, T[\text{K}] \tag{22}$$

With N simulations, one has $N-1$ burning time intervals but not the last one τ_{b_N} corresponding to the smallest diameter D_N. This last contribution can be simply neglected if D_N is sufficiently small. Otherwise, it is needed to approximate the evolution of $\dot{s}_{Al(B)}^{-1}$ in the interval $[0, D_N]$. Our numerical experiments show that the use of (21) with $\dot{s}_{Al(B)}^{-1} = 0$ at $D = 0$ may result in irregular variation of τ_b at small diameters. Instead, it is preferable to use the following function:

$$\dot{s}_{Al(B)}^{-1} = \alpha\, D^\beta \tag{23}$$

where α and β are determined by approximating $\dot{s}_{Al(B)}^{-1}$ in the interval $[D_N, D_{N-1}]$. The droplet density is assumed to be constant for diameters smaller than D_N. The burning time for the smallest diameter is defined by:

$$\tau_{b_N} = \frac{\rho_{Al(B)N}}{2} \int_0^{D_N} \alpha\, D^\beta dD = \frac{\rho_{Al(B)N}}{2} \frac{\alpha\, D_N^{\beta+1}}{\beta + 1} \tag{24}$$

After evaluating τ_{b_i} for different diameters D_i, it is possible to determine local values of n:

$$n_{loc,i} = \frac{\ln\left(\tau_{b_i}/\tau_{b_{i+1}}\right)}{\ln(D_i/D_{i+1})} \tag{25}$$

as well as the global value:

$$n = \frac{\sum_{i=1}^{N-1} n_{loc,i} \ln(D_i/D_{i+1})}{\sum_{i=1}^{N-1} \ln(D_i/D_{i+1})} = \frac{\ln\left(\tau_{b_1}/\tau_{b_N}\right)}{\ln(D_1/D_N)} \tag{26}$$

3. Validation case

The experimental case of Bucher et al. [9] is used to validate the modeling approach. A $210\,\mu\text{m}$ droplet is burning in an O_2/Ar atmosphere. The oxidizer conditions are: $P = 106$ kPa, $T = 300$ K, and $X_{O2} = 0.21$ balanced by Ar.

This case is first simulated with the 1D flow model by assuming nonreactive droplet surface. Reversible reactions (2) are considered for $Al_2O_3(L)$ generation in the gas phase. Thermal conductivity of gas is defined by formula (6) for this particular case. This simulation provided data on the surface conditions: mass flux of 0.853 kg/(s m^2) and temperature of 2655 K.

A 2D simulation is then performed with the Fluent 6.3 code with the same thermochemical and molecular transport models as in 1D including formula (6), for which a user-defined function was written. This latter remark is due to the fact that internally Fluent uses another formulation providing significantly different values of thermal conductivity. Boundary conditions on the droplet surface are specified by taking data on the mass flux and temperature from the 1D simulation. For the outer boundary situated at a distance of 100 droplet radii, the oxidizer conditions are imposed together with an axial velocity of 0.1 m/s. A structured computational mesh is composed of radial lines, uniformly distributed, and circular lines, whose radii are defined regarding the adapted grid in the 1D simulation. The flowfield is solved using the pressure-based formulation. The 3rd-order QUICK scheme is chosen for numerical approximation of convective fluxes and the SIMPLE scheme for pressure/velocity coupling.

Radial profiles of flow parameters obtained from the 2D simulation are affected by the oxidizer convection at a distance higher than $5\,r_p$ where r_p is the droplet radius. To take into account the convection effect on the windward side in 1D, the distance to the outer boundary is reduced to approximately $25\,r_p$.

Comparison between simulation results and experimental data from [9] is shown in Figure 1 for the profiles of temperature and normalized mole fraction of AlO and $Al_2O_3(L)$. The profiles from the 2D flowfield are extracted along the axis upstream (polar angle of 180°) and downstream (0°) from the droplet. Their comparison permits to verify that the oxidizer convection has no effect near the droplet. Within this zone, the 1D and 2D profiles are in a very good agreement. With the adjustment of the outer boundary position in 1D, the 1D results closely follow the 2D profiles on the windward side hence the effect of oxidizer convection is well reproduced. One can also note that the simulation results demonstrate good consistency with the experimental data.

a)

b)

c)
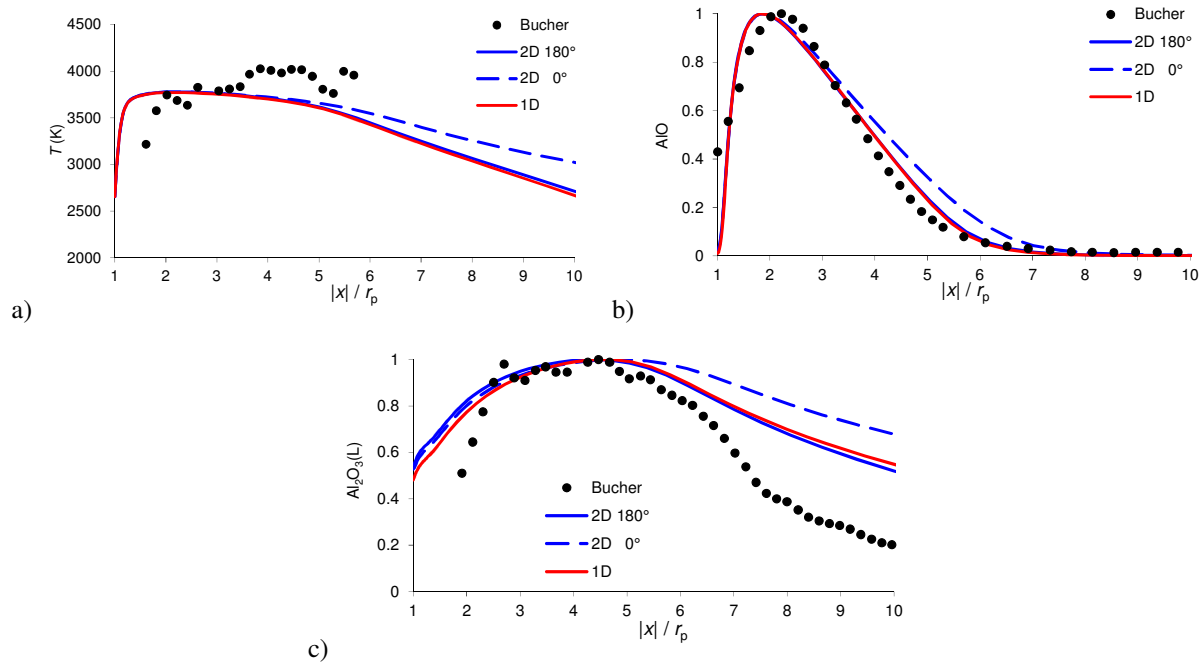
Figure 1 – Comparison of 1D and 2D simulation results with experimental data of Bucher et al. Profiles of temperature (a) and normalized mole fraction of AlO (b) and $Al_2O_3(L)$ (c) versus normalized radial distance.

4. Simulation results

4.1 O_2/Ar atmosphere

Aluminum droplet combustion is first simulated in an O_2/Ar atmosphere with 21% of O_2 by volume, $P = 1$ atm and $T = 300$ K. Oxidizer convection was not taken into account by setting the outer boundary at a distance of about $1000\,r_p$.

The results presented below permit to study the effect of the following two factors: i) surface reactivity and ii) reversibility of the gas-phase reactions generating $Al_2O_3(L)$. Three cases considered are summarized in Table 2. For case A, only one surface reaction enabling Al evaporation on the droplet surface is used whereas the complete kinetic mechanism is employed for cases B and C. For $Al_2O_3(L)$ production in the gaseous phase, reversible reactions (2) are used for cases A and B whereas irreversible reactions (1) are taken for case C.

Table 2 – Simulation cases in O_2/Ar atmosphere.

| Case	Surface reactions	$Al_2O_3(L)$ reactions
A	Evaporation	Reversible
B	All	Reversible
C	All	Irreversible

In Figure 2, the surface temperature and the mass consumption rate of bulk aluminum by surface reactions versus the droplet diameter are presented for the three cases. The effect of the surface reactions on the droplet temperature is observed in the whole diameter range and especially at smaller diameters ($D < 40$ µm). In case A,

Muller Mathieu, Davidenko Dmitry, Giovangigli Vincent

the droplet temperature starts rapidly decreasing when D is below 40 µm and the combustion finally stops at $D <$ 20 µm due to prevailing heat loss. In cases B and C, the droplet temperature increases until $D \approx$ 20 µm allowing stable combustion because the heat loss by evaporation is partially compensated by surface oxidation reactions. By comparing cases B and C, one can see that the reversibility of the $Al_2O_3(L)$ reactions has an impact on the surface temperature for large diameters ($D \geq$ 100 µm), this is because the flame temperature is higher at larger diameters as it will be demonstrated below.
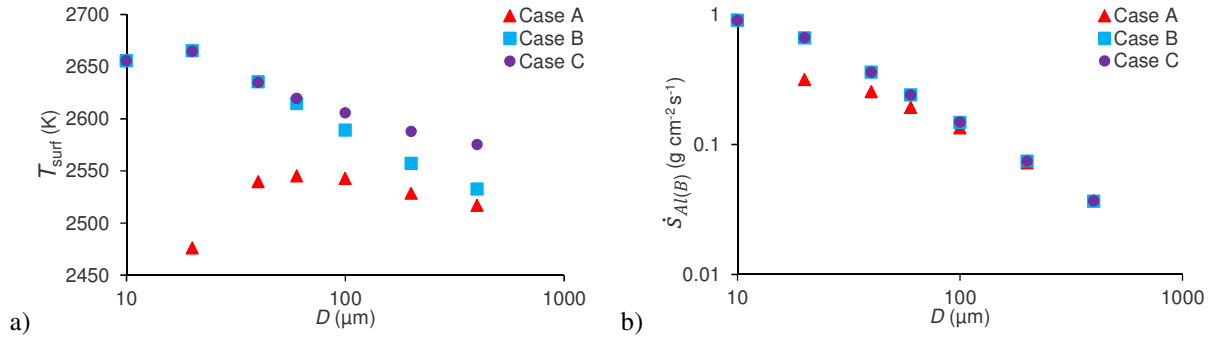
Figure 2 – Surface temperature (a) and mass consumption rate of bulk aluminum by surface reactions (b) versus droplet diameter for the O_2/Ar atmosphere.

The mass consumption rate of bulk aluminum is weakly dependent on the studied factors for $D \geq$ 100 µm. In spite of higher droplet temperature in cases B and C, the Al evaporation rate is not greater than in case A because the droplet is partially covered with oxides produced by surface reactions. For smaller diameters, the reduction of surface temperature in case A leads to significantly lower values of the consumption rate, which is only defined by the evaporation process. In cases B and C, the surface chemistry helps not only to maintain a high droplet temperature but also participates in aluminum oxidation resulting in production of bulk-phase alumina, which becomes important at small diameters.

In Figure 3, the burning time and local exponent defined by formula (25) are presented for the three cases. The burning time is also evaluated by Beckstead's correlation [10] by taking $n = 1.8$ and 2. One can observe that the simulation results follow well these empirical trends. In agreement with the results on the consumption rate of bulk aluminum in Figure 2b, the reversibility of the $Al_2O_3(L)$ reactions has negligible effect on the burning time and, as a consequence, on the local exponent of the D^n law. The difference in consumption rate explains why the burning time in case A is greater than in cases B and C for smaller diameters.

Considering the results on n_{loc}, one can observe that the surface chemistry has a fundamental effect on the droplet combustion. In case A, the local exponent is $n_{loc} \approx 1.9$ in the diameter range [200, 400] µm and decreases to ≈ 1.3 in the range [20, 40] µm. In cases B and C, n_{loc} varies from 2 to 1.8 when the diameter decreases from 400 to 40 µm and becomes ≈ 1.4 in the range [10, 20] µm. These results show an evolution from the diffusion-controlled regime with $n = 2$ towards the combustion regime controlled by heterogeneous kinetics with $n = 1$ when the droplet diameter decreases. This tendency was also found by Glorian et al. [3][5]. However in case A with a single evaporation reaction, this evolution begins at a much greater diameter than in cases B and C with the full surface chemistry.
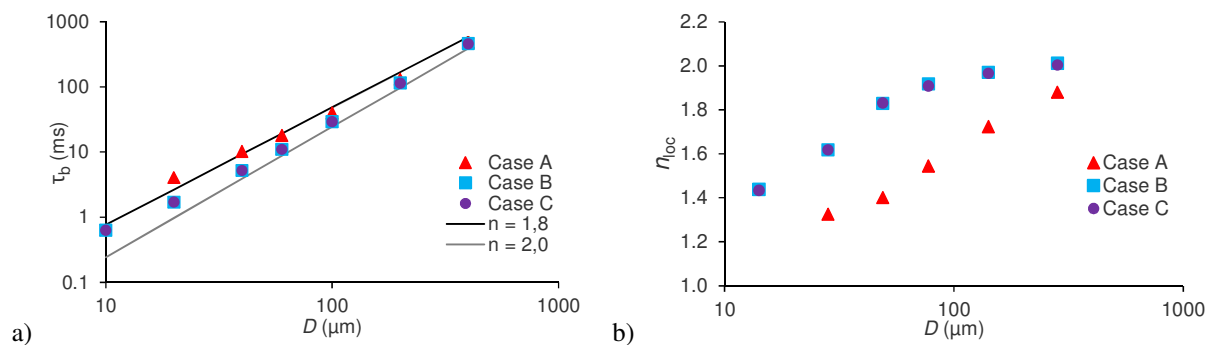

Figure 3 – Burning time (a) and local exponent of the D^n law (b) versus droplet diameter for the O_2/Ar atmosphere.

COMPUTATIONAL STUDY OF ALUMINUM DROPLET COMBUSTION IN DIFFERENT ATMOSPHERES

Table 3 – Global exponent of the D^n law for $D_0 = 400$ µm and the O_2/Ar atmosphere.

Case	This study	Glorian et al.
A	1.59	1.51
B, C	1.87	1.83

The results on global exponent of the D^n law for the initial diameter $D_0 = 400$ µm are summarized in Table 3 in comparison with the data by Glorian et al. [5]. The values of n for the same cases are conformal; the differences can be caused by several factors like the effect of oxidizer convection or the particularities of the transport model. In agreement with the results on n_{loc}, case A is characterized by significantly lower n than in cases B and C, for which n is close to the empirical value of 1.8 proposed by Beckstead.
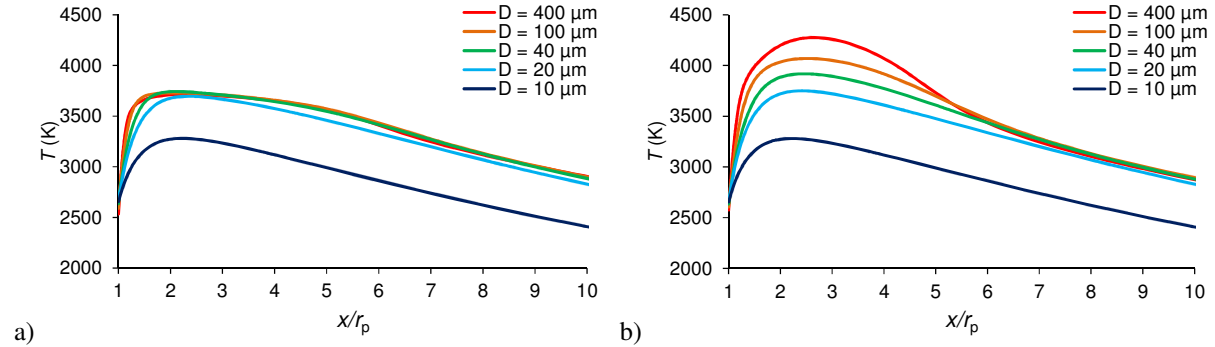
Figure 4 – Combustion in the O_2/Ar atmosphere. Profiles of temperature versus normalized radial distance for different droplet diameters in cases B (a) and C (b).
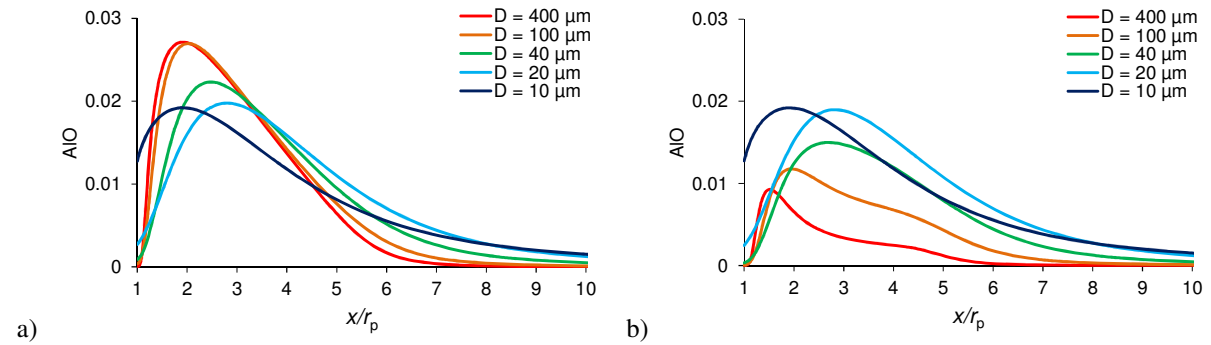
Figure 5 – Combustion in the O_2/Ar atmosphere. Profiles of AlO mole fraction versus normalized radial distance for different droplet diameters in cases B (a) and C (b).
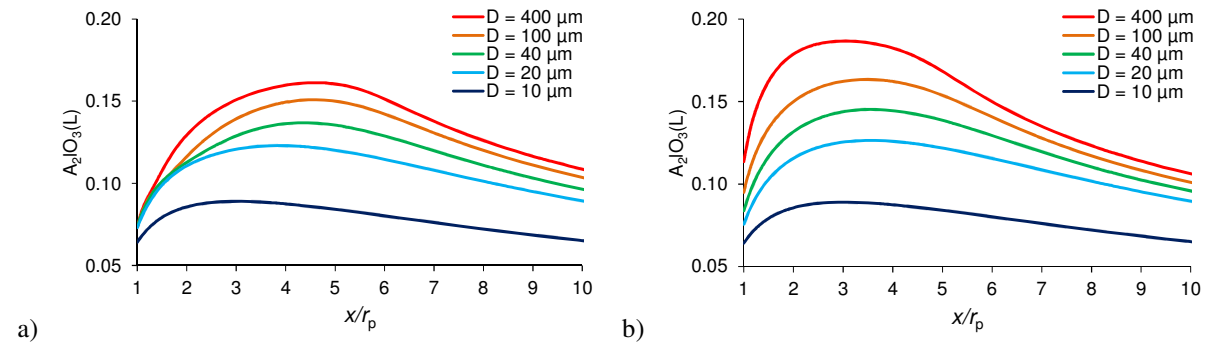
Figure 6 – Combustion in the O_2/Ar atmosphere. Profiles of $Al_2O_3(L)$ mole fraction versus normalized radial distance for different droplet diameters in cases B (a) and C (b).

In Figure 4, Figure 5 and Figure 6, the simulated profiles of temperature, mole fraction of AlO and mole fraction $Al_2O_3(L)$ are presented respectively for different droplet diameters corresponding to cases B and C. One can see from these graphs that the reversibility of the $Al_2O_3(L)$ reactions has an important effect on the flame for $D \geq$ 40 µm. The temperature profiles in Figure 4 show that with the reversible $Al_2O_3(L)$ reactions, the maximum

9

Muller Mathieu, Davidenko Dmitry, Giovangigli Vincent

temperature in the flame is effectively bounded by the dissociation limit to approximately 3710-3740 K whereas it can be far beyond this limit if the $Al_2O_3(L)$ reactions are treated as irreversible. The observed effect takes place in a limited zone near the droplet with $x/r_p < 6$, the temperature profiles being unaffected outside this zone. When the droplet diameter decreases, the temperature maximum approaches the droplet surface resulting in growth of thermal losses and, as a consequence, in global reduction of temperature in the flame. When the maximum temperature becomes lower than the dissociation limit, the rate of the backward reactions consuming $Al_2O_3(L)$ is too small compared to the forward rate and can be neglected. The relative difference of maximum temperature $\delta T_{max} = (T_{max,C} - T_{max,B})/T_{max,B}$ plotted versus the droplet diameter in Figure 7 shows that δT_{max} falls down below 1% at $D < 20$ µm.
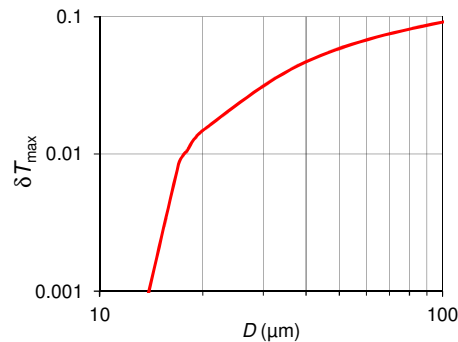
Figure 7 – Relative difference of maximum temperature between cases B and C versus droplet diameter.

The profiles of AlO and $Al_2O_3(L)$ mole fractions in Figure 5 and Figure 6 demonstrate strong differences between cases B and C for $D \geq 40$ µm. In case B, the AlO maximum is at the highest level for the largest diameter and both decrease together. In case C, the AlO maximum shows the opposite trend being at the lowest level for the largest diameter. The observed behavior is related to the $Al_2O_3(L)$ formation in the flame: the excessive production of $Al_2O_3(L)$ by the irreversible reactions in case C leads to strong consumption of AlO and, as a result, to much lower AlO fraction. In spite of important differences in absolute level between cases B and C, the maximum of $Al_2O_3(L)$ has a similar tendency to go down together with the droplet diameter. This is because the $Al_2O_3(L)$ production cannot compete with the $Al_2O_3(L)$ removal by the convective and diffusion transport.

As it was noted above, the droplet burns in the diffusion-controlled regime at $D \geq 40$ µm, which is confirmed by 0 level of AlO fraction at the droplet surface $x/r_p = 1$ in Figure 5. By comparing the AlO profiles for $D = 40$, 20 and 10 µm, one can identify a clear transition towards the kinetically-controlled combustion regime, which is characterized by increasing AlO fraction at the surface. One can also see a relatively rapid global decrease of temperature and $Al_2O_3(L)$ fraction when the diameter changes from 20 to 10 µm.

4.2 H_2O atmosphere

The conditions for the H_2O atmosphere are chosen the same as in the study of Glorian et al. [5]. Pure H_2O is considered in vapor phase at $T = 300$ K and two pressures $P = 1$ and 10 atm. Even if these conditions are fully artificial, they can be used to examine the behavior of the reacting system and to compare our results with those from [5].

A comparison with the results of Glorian et al. [5] is made for a droplet diameter of 220 µm and $P = 1$ atm. The case presented in [5] was simulated with a convection speed of 0.5 m/s. With the 1D approach, it is necessary to adjust the position of the outer boundary to have a comparable extent of the temperature profile. The obtained profiles of temperature and AlO mole fraction are plotted in Figure 8 together with the profiles from [5]. The compared temperature profiles are conformal however the temperature level obtained in this study is greater by approximately 200 K near the droplet. These discrepancies can be, on the one hand, due to the different formulations of the diffusion mass flux and thermal conductivity of gas and, on the other hand, due to some 2D effects that cannot be properly modeled with the 1D approach. The AlO profiles are of similar shape but the peak is twice higher in this study than in [5]. As it will be demonstrated by the temperature and AlO profiles presented below, the AlO peak is very temperature-sensitive so the observed difference between the AlO profiles in Figure 8 is mainly due to the mismatch in the maximum temperature.
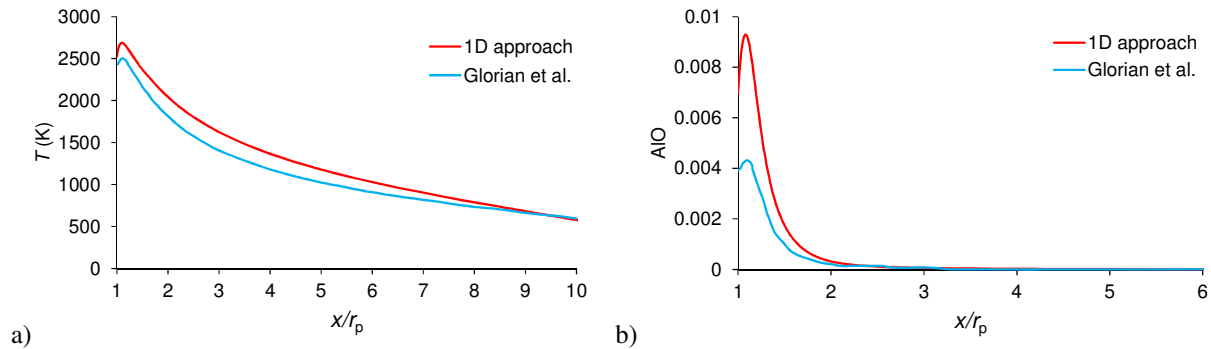
10

COMPUTATIONAL STUDY OF ALUMINUM DROPLET COMBUSTION IN DIFFERENT ATMOSPHERES

Figure 8 – Combustion of a droplet with D = 220 µm in the H_2O atmosphere at P = 1atm.
Profiles of temperature (a) and AlO mole fraction (b) obtained in this study and by Glorian et al.

Both graphs in Figure 8 show that combustion is restricted to a narrow zone near the droplet surface with a weak temperature peak and an important level of AlO fraction at the droplet surface. In the present study, it is found that two different combustion regimes can be obtained under the same conditions. The following results are obtained for different droplet diameters $D \leq 400$ µm. Reversible formulations (2) are used for the $Al_2O_3(L)$ reactions but the effect of reversibility is much less important than for the O_2/Ar atmosphere because the maximum temperature is not strongly limited by dissociation. Oxidizer convection is not taken into account by setting the outer boundary at a distance of about 1000 r_p.

To discriminate the combustion regimes obtained with the 1D approach, they will be called "surface" when the temperature profile is similar to those presented in Figure 8 and "gaseous" when the temperature maximum is much higher than the surface temperature and situated at a significant distance from the droplet. Both combustion regimes are characterized by the diameter range, burning time and D^n law exponent in Table 4. The gaseous regime is restricted to a certain diameter, below which only the surface regime can exist. One can see that this lower diameter limit depends on the pressure and is strongly relaxed by changing P from 1 to 10 atm. On the contrary, an upper diameter limit is found for the surface regime at 10 atm. The burning time and D^n law exponent are evaluated for the initial diameter D_0 = 400 µm by taking data for the corresponding combustion regime in combination with the other one in order to complete the range of D. For example at 1 atm, the data for the gaseous regime in the diameter range [160, 400] µm are completed with the data for the surface regime in the range [28, 159] µm. The gaseous regime results in more intense combustion and a shorter burning time. The n values are relatively close for both regimes and vary approximately from 1.8 to 2 when the pressure increases. In the gaseous regime, aluminum oxidation by surface reactions is almost negligible whereas it is as high as 10-20% in the surface regime for the same diameter, so the oxidation process takes place mainly in the gaseous phase for both regimes. Hence the so-called surface regime cannot be directly associated with the kinetically-controlled regime in terms of the combustion theory. Transition towards the kinetically-controlled combustion is observed for small droplet diameters when oxidation by surface reactions plays an important role in the overall consumption of bulk aluminum.

Table 4 – Pressure, combustion regime, droplet diameter range,
burning time and D^n law exponent (D_0 = 400 µm) for the H_2O atmosphere.

P (atm)	Regime	D (µm)	τ_b (ms)	n
1	Gaseous	[160, 400]	234	1.72
	Surface	[28, 400]	266	1.77
10	Gaseous	[22, 400]	167	1.97
	Surface	[10, 125]	171	1.95

The surface and gaseous regimes can be compared by considering the plots in Figure 9 to Figure 11 for P = 1 atm and in Figure 12 to Figure 14 for P = 10 atm. The temperature profiles in Figure 9 and Figure 12 and the AlO mole fraction profiles in Figure 10 and Figure 13 demonstrate globally similar trends for each combustion regime when the droplet diameter decreases. The pressure has an important effect on the flame temperature, which increases significantly for both regimes when the pressure changes from 1 to 10 atm.

In the surface regime, all the temperature profiles are similar and characterized by a weakly marked peak situated very close to the droplet surface. One can observe that in this particular regime, the overall temperature

11

Muller Mathieu, Davidenko Dmitry, Giovangigli Vincent

level grows up when the droplet diameter decreases resulting in almost equidistant profiles; the temperature growth is accompanied by an important increase of the AlO peak, which is also very near the droplet surface. The AlO fraction at the surface is close to the peak value.
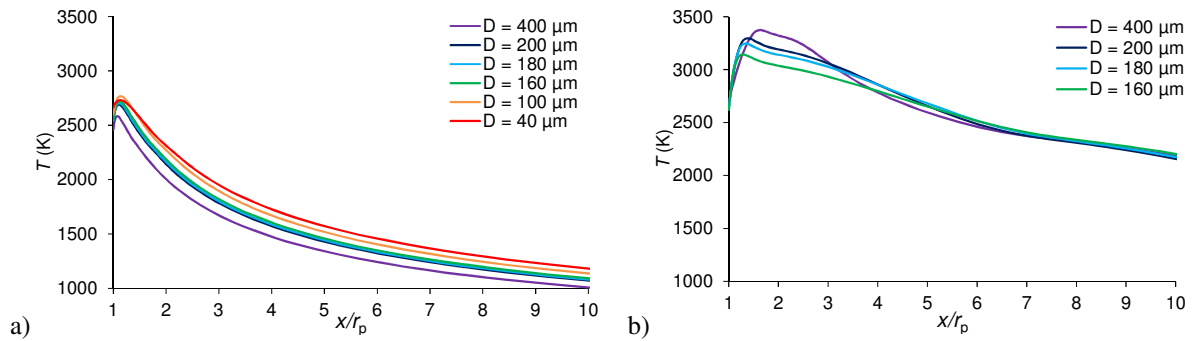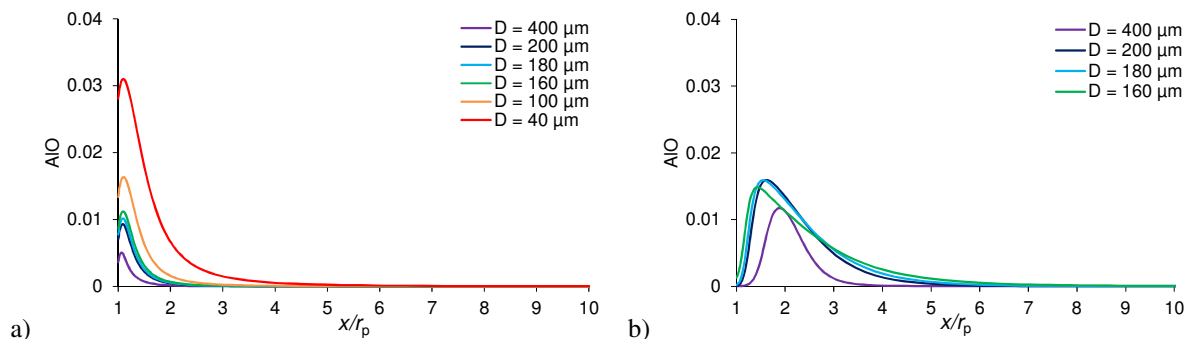

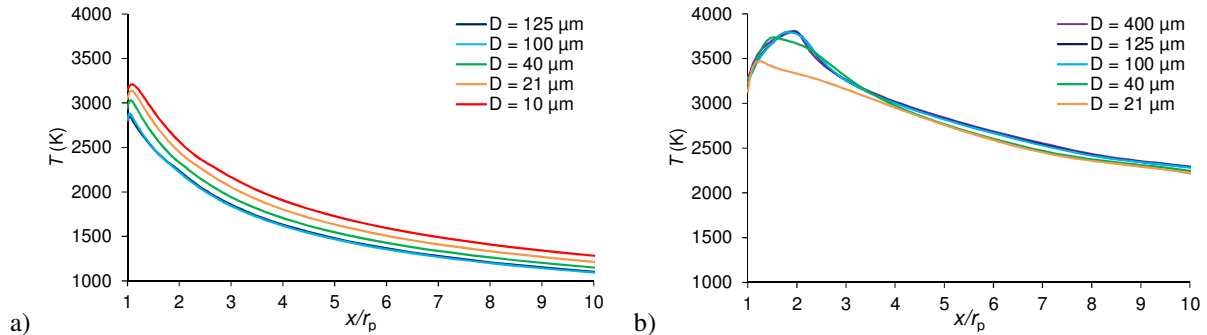Figure 9 – Combustion in the H_2O atmosphere at P = 1 atm. Profiles of temperature versus normalized radial distance for different droplet diameters: a) surface regime; b) gaseous regime.
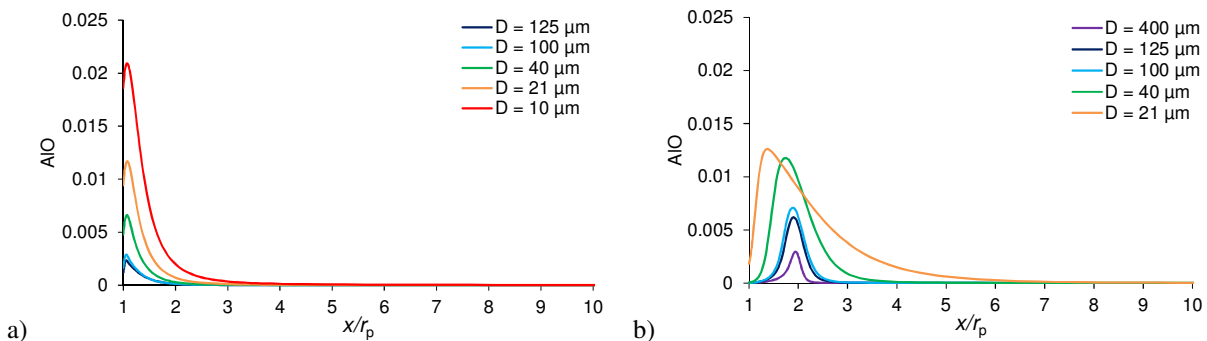

Figure 10 – Combustion in the H_2O atmosphere at P = 1 atm. Profiles of AlO mole fraction versus normalized radial distance for different droplet diameters: a) surface regime; b) gaseous regime.
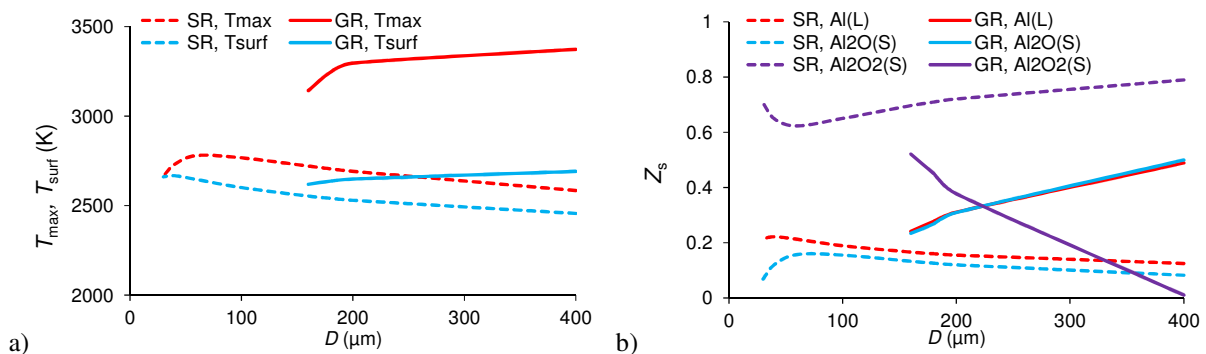
Figure 11 – Combustion in the H_2O atmosphere at P = 1 atm. Maximum and surface temperature (a) and surface species site fractions (b) versus droplet diameter for the surface (SR) and gaseous (GR) combustion regimes.

In the gaseous regime, the temperature is much higher in overall level and its maximum reaches the dissociation limit at about 3630 K for P = 10 atm. With the decrease of D, the temperature maximum has a tendency to diminish and move closer to the surface in terms of normalized distance. The maximum AlO fraction is not so strongly affected by the diameter change. The AlO fraction at the surface remains at 0 level for larger diameters and slightly increases for the limiting diameter.

The maximum temperature T_{max} and surface temperature T_{surf} are plotted versus the droplet diameter in Figure 11a for P = 1 atm and in Figure 14a for P = 10 atm. These plots show that T_{surf} is significantly greater in the gaseous regime than in the surface one and that the difference $T_{max} - T_{surf}$ remains almost constant in wide ranges of D for both regimes. At the limiting diameter of the gaseous regime, T_{max} and T_{surf} tend to join the respective curves of the surface regime.

Figure 11b and Figure 14b present the variation of the site fractions Z_s of major surface species as a function of

D for both regimes. The strong difference between the surface species fractions can explain the existence of the two distinct regimes. The surface regime is characterized by the dominance of the $Al_2O_2(S)$ oxide and a relatively low level of $Al(L)$. Low surface concentration of $Al(L)$ limits Al evaporation and leads to a weak flame corresponding to the surface regime. At a sufficiently high surface concentration of $Al(L)$, intense evaporation of Al can feed up a stronger flame of the gaseous regime.

Figure 12 – Combustion in the H_2O atmosphere at $P = 10$ atm. Profiles of temperature versus normalized radial distance for different droplet diameters: a) surface regime; b) gaseous regime.

Figure 13 – Combustion in the H_2O atmosphere at $P = 10$ atm. Profiles of AlO mole fraction versus normalized radial distance for different droplet diameters: a) surface regime; b) gaseous regime.
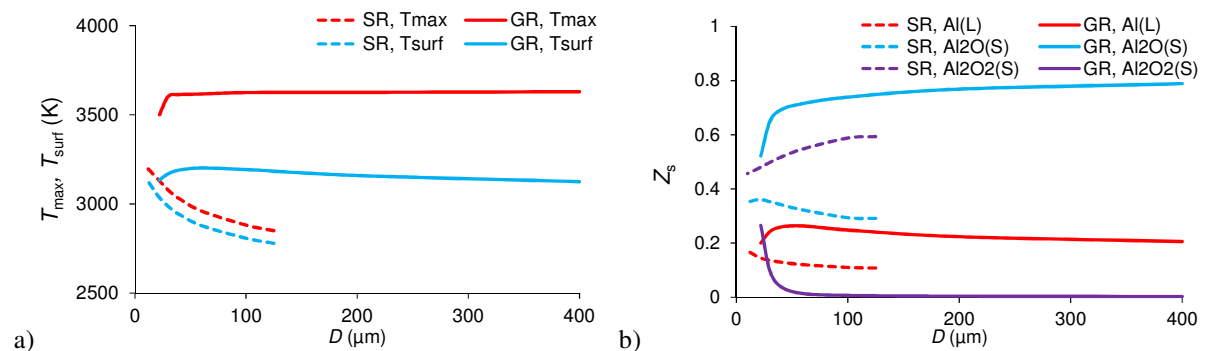

Figure 14 – Combustion in the H_2O atmosphere at $P = 10$ atm. Maximum and surface temperature (a) and surface species site fractions (b) versus droplet diameter for the surface (SR) and gaseous (GR) combustion regimes.

The pressure change has an important impact on the surface species. In the gaseous regime at 1 atm, $Al(L)$ and $Al_2O(S)$ fractions are equal and follow the same trend and their variation is balanced by $Al_2O_2(S)$; at 10 atm, $Al_2O(S)$ becomes dominant and balances the variation of $Al(L)$ while $Al_2O_2(S)$ remains at 0 level. This different behavior is also caused by the change in the surface temperature, which is among the main factors defining the equilibrium concentrations of the surface species. The proof can be found by analyzing the graphs in Figure 14 for the gaseous regime: when the surface temperature decreases near the lower limit of droplet diameter, one can see a quick response of the $Al_2O(S)$ and $Al_2O_2(S)$ fractions.

Muller Mathieu, Davidenko Dmitry, Giovangigli Vincent

4.3 CO_2 atmosphere

The conditions for the CO_2 atmosphere are chosen by analogy with the H_2O one, i.e. pure species at $T = 300$ K and two pressures $P = 1$ and 10 atm. Simulation results for the same conditions were presented by Glorian et al. [5].

A similar comparison as for the H_2O atmosphere is made with the results of Glorian et al. [5] for a droplet diameter of 220 µm and $P = 1$ atm. The gas-phase reactions generating $Al_2O_3(L)$ are treated as irreversible in accordance with the models used in [5]. The obtained profiles of temperature and AlO mole fraction are plotted in Figure 15 together with the profiles from [5]. The compared temperature profiles are conformal however the maximum temperature level obtained in this study is lower by approximately 200 K. For the AlO profiles, the maximum levels are comparable but there is no strong peak near the droplet surface as for the profile from [5]. The same explanations as for the case of H_2O atmosphere can be proposed concerning the observed discrepancies.
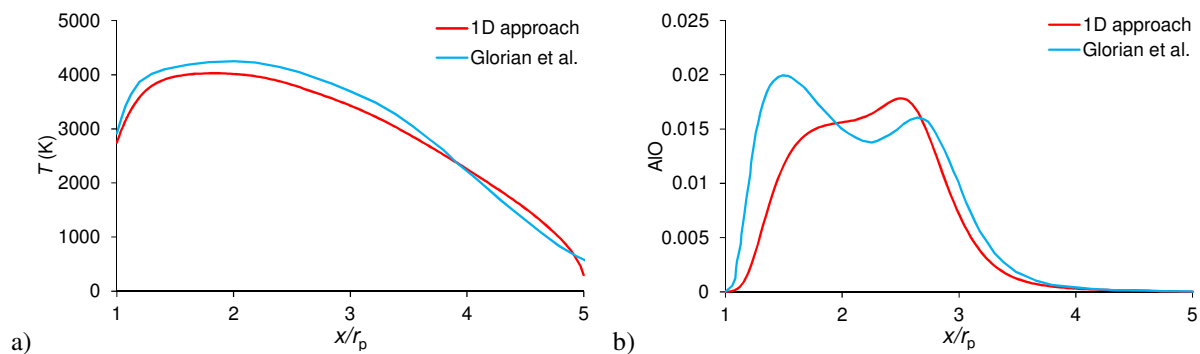

Figure 15 – Combustion of a droplet with $D = 220$ µm in the CO_2 atmosphere at $P = 1$atm. Profiles of temperature (a) and AlO mole fraction (b) obtained in this study and by Glorian et al.

Aluminum combustion in the CO_2 atmosphere produces a high-temperature flame, which can be strongly affected by dissociation of combustion products. The following results are obtained for different droplet diameters $D \leq 400$ µm. Reversible and irreversible formulations are considered for the $Al_2O_3(L)$ reactions. As for the cases presented above, oxidizer convection is not taken into account by setting the outer boundary at a distance of about 1000 r_p.

The results on the burning time and D^n law exponent for the initial diameter $D_0 = 400$ µm are summarized in Table 5. The burning time is reduced when the pressure increases or irreversible $Al_2O_3(L)$ reactions are used because both factors result in a growth of temperature in the flame and at the droplet surface. With the reversible $Al_2O_3(L)$ reactions, the D^n law exponent is close to 1.8 for both pressure levels whereas with the irreversible reactions, it grows approximately from 1.7 to 2

Table 5 – Pressure, reversibility of $Al_2O_3(L)$ reactions, burning time and D^n law exponent ($D_0 = 400$ µm) for the CO_2 atmosphere.

P (atm)	$Al_2O_3(L)$ reactions	τ_b (ms)	n
1	Reversible	150	1.81
	Irreversible	133	1.73
10	Reversible	94	1.81
	Irreversible	87	1.95

The radial profiles of temperature an AlO mole fraction corresponding to different droplet diameters are presented in Figure 16 and Figure 17 for $P = 1$ atm as well as in Figure 19 and Figure 20 for $P = 10$ atm. The observed behavior for the two pressure levels is globally similar and one can also note that they resemble to the profiles obtained for the O_2/Ar atmosphere (see Figure 4 and Figure 5). With the reversible $Al_2O_3(L)$ reactions, the maximum temperature is strongly limited by dissociation to about 3680 K at 1 atm and to values varying from 4040 to 3930 K depending on the droplet diameter at 10 atm; the AlO profile has a single peak and a tendency to decrease together with the diameter. With the irreversible $Al_2O_3(L)$ reactions, the temperature maximum is much higher and exceeds 5000 K at 10 atm, which seems to be unphysical; as for the O_2/Ar

atmosphere, the excessive production of $Al_2O_3(L)$ by the irreversible reactions leads to strong consumption of AlO and, as a result, to low AlO profiles with two peaks in some cases.
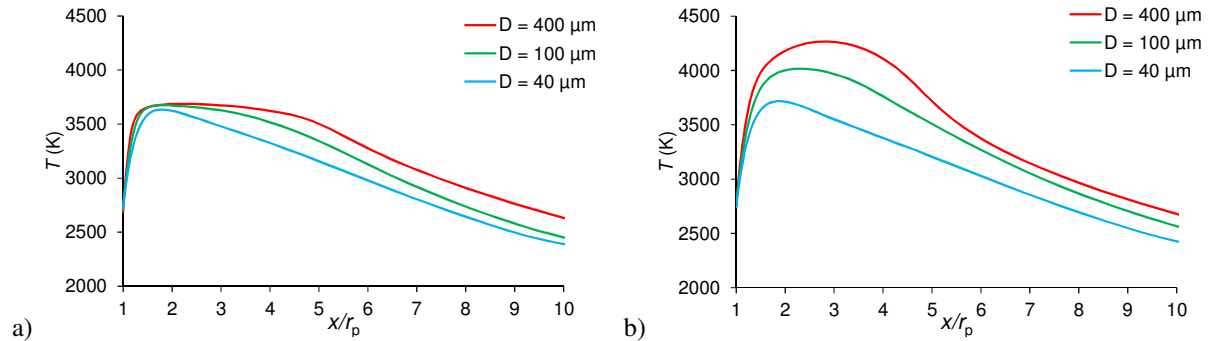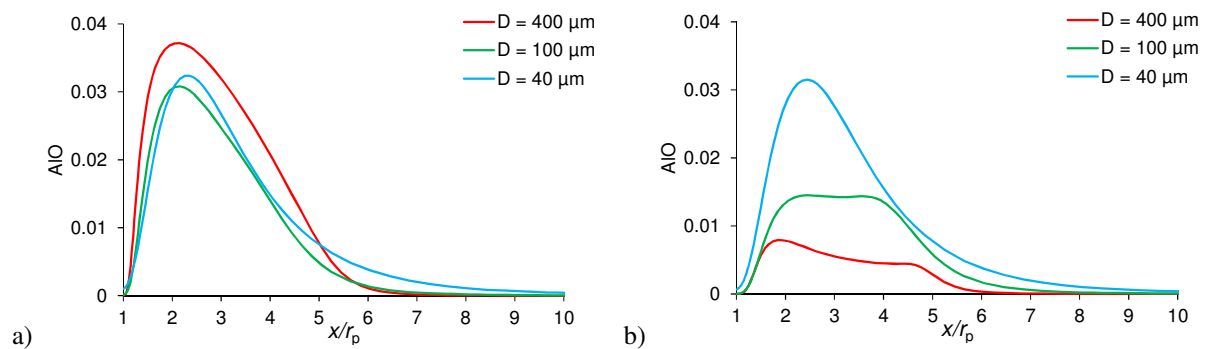

Figure 16 – Combustion in the CO_2 atmosphere at $P = 1$ atm. Profiles of temperature versus normalized radial distance for different droplet diameters and reversible (a) or irreversible (b) $Al_2O_3(L)$ reactions.

Figure 17 – Combustion in the CO_2 atmosphere at $P = 1$ atm. Profiles of AlO mole fraction versus normalized radial distance for different droplet diameters and reversible (a) or irreversible (b) $Al_2O_3(L)$ reactions.
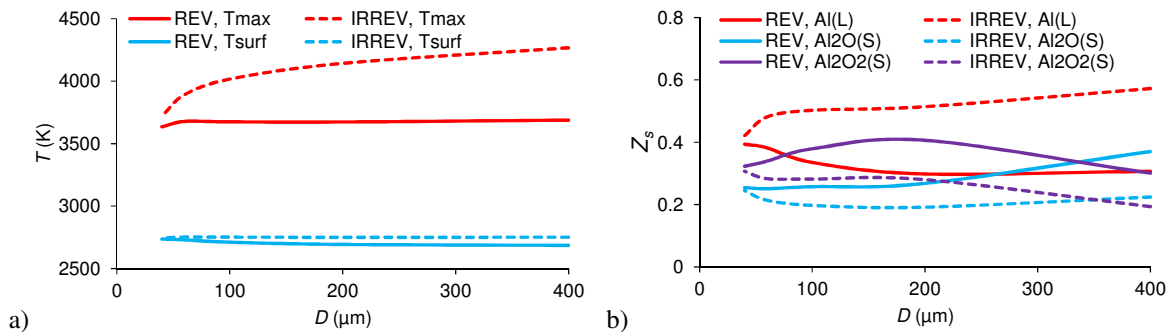

Figure 18 – Combustion in the CO_2 atmosphere at $P = 1$ atm. Maximum and surface temperature (a) and surface species site fractions (b) versus droplet diameter for reversible (REV) and irreversible (IRREV) $Al_2O_3(L)$ reactions.

The maximum temperature T_{max} and surface temperature T_{surf} are plotted versus the droplet diameter in Figure 18a for $P = 1$ atm and in Figure 21a for $P = 10$ atm. These plots show that T_{surf} remains almost constant in the whole range of diameter variation and is influenced by the flame temperature change with the different formulations of the $Al_2O_3(L)$ reactions.

Figure 18b and Figure 21b present the variation of the site fractions Z_s of major surface species as a function of D for both formulations of the $Al_2O_3(L)$ reactions. Some common features with results presented for the H_2O atmosphere (see Figure 11b and Figure 14b) can be noted, in particular the relative change of the $Al_2O(S)$ and $Al_2O_2(S)$ fractions caused by the pressure rise and the corresponding increase in the surface temperature. Another important effect can be attributed to the change in the gas composition caused by the different formulations of the $Al_2O_3(L)$ reactions. With the irreversible $Al_2O_3(L)$ reactions, aluminum suboxides are depleted by the gas-phase reactions responsible for $Al_2O_3(L)$ production, so a strong reduction of $Al_2O(S)$ and $Al_2O_2(S)$ fractions is observed whereas the $Al(L)$ fraction is correspondingly increased.

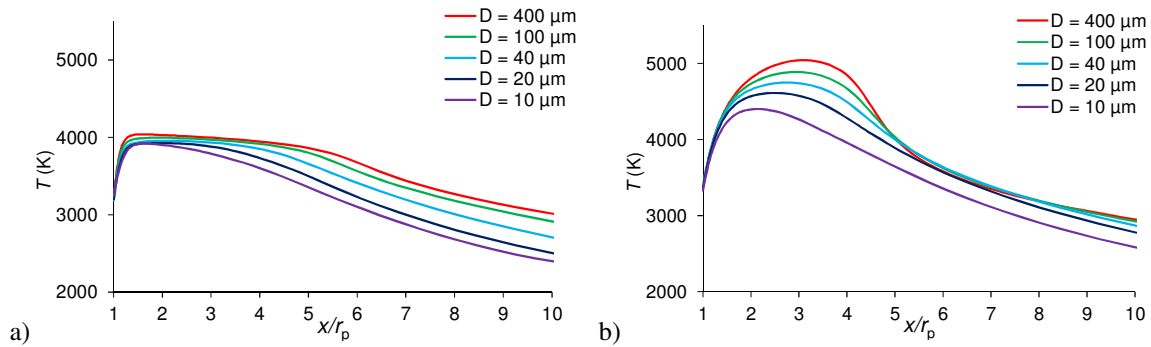Muller Mathieu, Davidenko Dmitry, Giovangigli Vincent

Figure 19 – Combustion in the CO_2 atmosphere at P = 10 atm. Profiles of temperature versus normalized radial distance for different droplet diameters and reversible (a) or irreversible (b) $Al_2O_3(L)$ reactions.
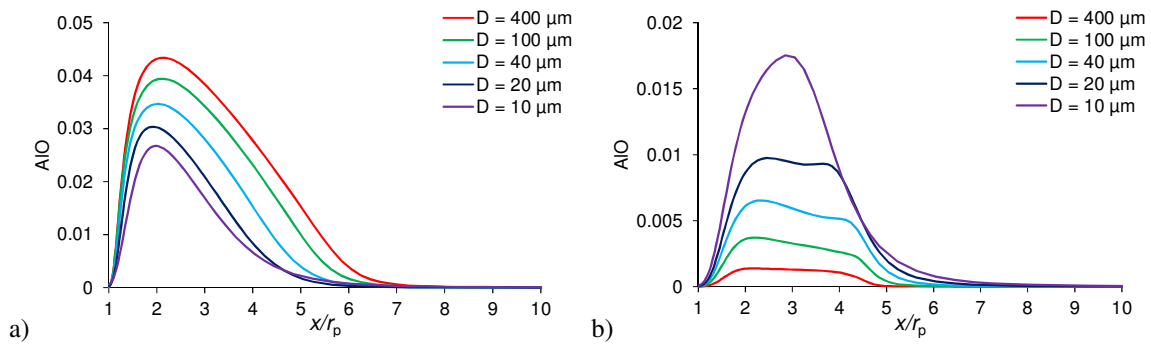

Figure 20 – Combustion in the CO_2 atmosphere at P = 10 atm. Profiles of AlO mole fraction versus normalized radial distance for different droplet diameters and reversible (a) or irreversible (b) $Al_2O_3(L)$ reactions.
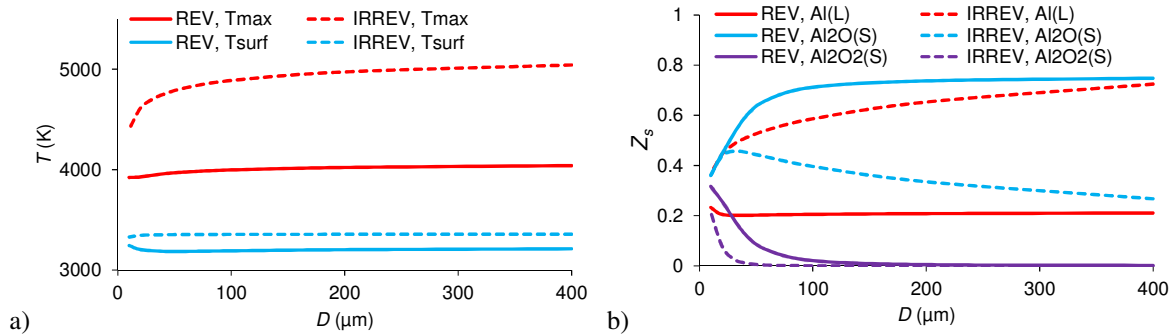

Figure 21 – Combustion in the CO_2 atmosphere at P = 10 atm. Maximum and surface temperature (a) and surface species site fractions (b) versus droplet diameter for reversible (REV) and irreversible (IRREV) $Al_2O_3(L)$ reactions.

5. Conclusions

A 1D combustion model for an aluminum droplet with detailed thermochemical and transport models has been developed at ONERA and validated with respect to the 2D axisymmetric approach under conditions corresponding to the experience of Bucher et al. [9] in the O_2/Ar atmosphere. A possibility of taking into account the effect of oxidizer convection by adjusting the outer boundary position has been demonstrated providing excellent agreement between the 1D and 2D results as well as good conformity with the reference experimental data.

An important parametric study has been conducted by simulating quasi-steady-state combustion of droplets with different diameters $D \leq 400\,\mu m$ in three atmospheres (O_2/Ar, pure H_2O and CO_2) at two pressure levels (1 and 10 atm). Effects due to the surface chemistry model and the reversibility of the gas-phase reactions producing $Al_2O_3(L)$ have been investigated. The burning time and exponent of the D^n law have been evaluated for the considered physical conditions and modeling options. Profiles of temperature and mole fractions of important species have been presented and analyzed. The obtained results correspond mainly to the diffusion-controlled combustion regime for which the n exponent varies from 1.8 to 2. For small diameters on the order of 10 µm, the

16

simulation results show a transition towards the combustion regime controlled by the heterogeneous kinetics. In the case of O_2/Ar atmosphere, this transition starts at larger diameters if only Al evaporation is modeled on the droplet surface compared to the simulations with the full surface chemistry.

Effects due to the reversibility of the Al_2O_3(L) reactions are found very important for the O_2/Ar and CO_2 atmospheres. With the reversible Al_2O_3(L) reactions, the maximum temperature in the flame is effectively restricted to the dissociation limit whereas with the irreversible reactions, flame temperature can be unphysically high; in addition, AlO fraction in the flame is strongly reduced with the latter assumption.

For the H_2O atmosphere, two combustion regimes have been identified: one with the flame temperature much higher than the droplet temperature and another with a weak temperature peak near the droplet surface. Both regimes can coexist in some range of droplet diameter depending on the pressure level. These regimes are characterized as diffusion-controlled however the second one features more important aluminum oxidation by the surface reactions.

The 1D approach presented in this paper provided important results for the studied atmospheres and seems to be suitable for modelling the aluminum combustion in a solid rocket motor, which will be conducted in future.

6. Acknowledgments

References

[1] Beckstead, M.W., Liang, Y., Pudduppakkam, K.V. 2005. Numerical simulation of single aluminum particle combustion. *Combustion, Explosion and Shock Waves*. 41(6):622–638.

[2] Washburn, E.B., Trivedi, J.N., Catoire, L., Beckstead, M.W. 2008. The simulation of the combustion of micrometer-sized aluminum particles with steam. *Combustion Science and Technology*. 180(8):1502-1517.

[3] Glorian, J. 2014. Cinétique hétérogène pour la combustion de l'aluminium. PhD thesis of ENSTA PariTech.

[4] Glorian, J., Catoire, L., Gallier, S., Cesco, N. 2015. Gas-surface thermochemistry and kinetics for aluminum particle combustion. *Proceedings of the Combustion Institute*. 35(2):2439–2446.

[5] Glorian, J., Gallier, S., Catoire, L. 2016. On the role of heterogeneous reactions in aluminum combustion. *Combustion and Flame*. 168:378-392.

[6] Orlandi, O., Fabignon, Y. 2000. Numerical simulation of the combustion of a single aluminum particle in air. *5th International Symposium on Special Topics in Chemical Propulsion*. Stresa, Italy.

[7] Orlandi, O. 2002. Modélisation et simulation numérique de la combustion d'une goutte isolée d'aluminium. PhD thesis of the University of Orléans.

[8] Cho, S.Y., Yetter, R.A., Dryer, F.L. 1992. A computer model for one-dimensional mass and energy transport in and around chemically reacting particles, including complex gas-phase chemistry, multicomponent molecular diffusion, surface evaporation, and heterogeneous reaction. *Journal of Computational Physics*. 102:160-179.

[9] Bucher, P., Yetter, R.A., Dryer, F.L., Parr, T.P., Hanson-Parr, D.M. 1998. PLIF species and radiometric temperature measurements of aluminum particle combustion in O_2, CO_2 and N_2O oxidizers, and comparison with model calculations. *27th Symposium on Combustion*. The Combustion Institute. pp.2421-2429.

[10] Beckstead, M.W. 2004. A summary of aluminum combustion. *RTO/VKI Special Course on Internal Aerodynamics in Solid Rocket Propulsion*. RTO-EN-023.

[11] Ern, A., Giovangigli, V. 1994. Multicomponent Transport Algorithms. *Lectures Notes in Physics*. 24 Springer-Verlag. Berlin.

[12] Ern, A., Giovangigli, V. 1995. Fast and accurate multicomponent transport property evaluation. *Journal of Computational Physics*. 120:105–116.

[13] Marion, M., Chauveau, C., Gökalp, I. 1996. Studies on the ignition and burning of levitated aluminum particles. *Combustion Science and Technology*. 115(4-6):369-390.